

# Derivation of Instrument Requirements for Polarimetry using Mg, Fe, and Mn lines between 250 and 290 nm

A.G. DE WIJN,<sup>1</sup> P.G. JUDGE,<sup>1</sup> R. EZZEDDINE,<sup>2</sup> AND A. SAINZ DALDA<sup>3,4</sup>

<sup>1</sup>High Altitude Observatory, National Center for Atmospheric Research, P.O. Box 3000, Boulder, CO 80307, USA

<sup>2</sup>Department of Astronomy, University of Florida, 211 Bryant Space Sciences Center, Gainesville, Florida, 32611, USA

<sup>3</sup>Lockheed Martin Solar & Astrophysics Laboratory, 3251 Hanover Street, Palo Alto, CA 94304, USA

<sup>4</sup>Bay Area Environmental Research Institute, NASA Research Park, Moffett Field, CA 94035, USA.

## Abstract

Judge et al. (2021) recently argued that a region of the solar spectrum in the near-UV between about 250 and 290 nm is optimal for studying magnetism in the solar chromosphere due to an abundance of Mg II, Fe II, and Fe I lines that sample various heights in the solar atmosphere. In this paper we derive requirements for spectropolarimetric instruments to observe these lines. We derive a relationship between the desired sensitivity to magnetic field and the signal-to-noise of the measurement from the weak-field approximation of the Zeeman effect. We find that many lines will exhibit observable polarization signals for both longitudinal and transverse magnetic field with reasonable amplitudes.

*Unified Astronomy Thesaurus concepts:* Polarimeters (1277); Solar instruments (1499); Spectropolarimetry (1973); Solar chromosphere (1479)

## 1. Introduction

The region between 250 and 290 nm of the solar spectrum contains the well-known Mg II h and k lines but also a large number of Fe I and Fe II lines. In particular, there are many strong Fe II lines that sample various heights in the solar atmosphere. Judge et al. (2021) argue that these lines are highly promising for studying magnetism in the solar chromosphere based on a broad evaluation of possible diagnostics of magnetic field in the solar chromosphere. In order to evaluate the practical use of this region of the spectrum, they analyzed the signal levels expected in the Mg II k line by synthesizing polarized spectra using the HanleRT code (del Pino Alemán et al. 2020) over a grid of line-of-sight angles and magnetic field strengths for a given field inclination and azimuth angle. They find that the combined Hanle and Zeeman effects produce measurable signals for this line in many geometries. In particular, they note that diagnostics of vector field with strengths of 5 to 50 G are achievable for observation angles greater than 45°, as a result of the Hanle effect in Stokes  $Q$  and  $U$ .

However, they do not evaluate *observability* of magnetic field diagnostics using the many Fe II lines, which underpin the value of this region of the spectrum for diagnostics of magnetic field in the chromosphere. In this paper we evaluate the signal-to-noise ratio (SNR) required to observe a signa-

ture of longitudinal or transverse magnetic field with a given field strength under the assumption of the weak-field approximation of the Zeeman effect. We do not treat the Hanle effect in our study. Judge et al. (2021) note that work on the Hanle effect in the Fe II lines is underway, and will be reported elsewhere. However, the Stokes  $V$  signal is unaffected by the Hanle effect, and therefore the signal strength of the longitudinal component of the magnetic field can be estimated using the methods in this paper. In addition, many science cases will require observations on the disk or of magnetic field with strengths considerably exceeding the critical Hanle field strength. In those situations, the Hanle effect has a negligible contribution to the polarization signal, and therefore the methods used in this paper apply.

We will first discuss briefly the weak-field approximation and its applicability, and then derive formulae to relate the error on a measurement of the magnetic field to the SNR of an observation for both the longitudinal and transverse components. We will derive parameters in several different ways to illustrate possible ways one may approach a similar problem for other spectral lines. Finally, for specific lines in this particular spectral region, we will investigate the instrumental effect of limited spectral resolution, and illustrate the method through an example calculation.

## 2. Analysis

The Zeeman splitting of a spectral line is given by

$$\Delta\lambda_B = s B \lambda_0^2, \quad (1)$$

where  $B$  is the magnetic field strength and  $\lambda_0$  is the rest wavelength of the line. We here work with vacuum wave-

lengths in units of nm and the magnetic flux density  $B$  in units of G, and therefore have  $s = 4.67 \times 10^{-11} \text{ nm}^{-1} \text{ G}^{-1}$ .

If the Zeeman splitting is much smaller than the Doppler width of the line, it is possible to apply a perturbative scheme to the radiative transfer equations and derive expressions for the circular and linear polarization signals in terms of the first and second derivative of the intensity profile, respectively (Landi Degl'Innocenti & Landi Degl'Innocenti 1973). Landi Degl'Innocenti & Landolfi (2004) note that for iron lines in the visible spectrum that sample the photosphere, this approximation is valid up to kG field strengths. At shorter wavelengths, the weak-field approximation is applicable for stronger field strengths because Zeeman splitting scales with the square of the wavelength, while Doppler broadening scales linearly. In addition, lines that form in the chromosphere have larger Doppler broadening than those that form in the photosphere. For these reasons we can safely assume the weak-field approximation is applicable for magnetic field up to at least kG strength for the lines we consider here.

The circular and linear polarization signals as a function of wavelength are

$$V(\lambda) = -\Delta\lambda_B \bar{g} \frac{\partial I(\lambda)}{\partial \lambda} \cos \theta, \quad (2)$$

$$L(\lambda) = -\frac{1}{4} \Delta\lambda_B^2 \bar{G} \frac{\partial^2 I(\lambda)}{\partial \lambda^2} \sin^2 \theta, \quad (3)$$

where  $\bar{g}$  and  $\bar{G}$  are the effective Landé factors for longitudinal and transverse magnetic field, respectively,  $I(\lambda)$  is the intensity, and  $\theta$  is the inclination of the magnetic field with respect to the line-of-sight. For convenience, we write  $B_{\parallel} = B \cos \theta$  and  $B_{\perp} = B \sin \theta$ .

An interpretation of the Stokes profiles effectively combines the signal over a wavelength range  $\Delta\lambda$ . We are therefore interested in the integrated absolute signals  $\mathcal{V}$  and  $\mathcal{L}$ ,

$$\begin{aligned} \mathcal{V} &= \int_{\Delta\lambda} |V(\lambda)| \\ &= s \bar{g} \lambda_0^2 |B_{\parallel}| \int_{\Delta\lambda} \left| \frac{\partial I(\lambda)}{\partial \lambda} \right| d\lambda, \end{aligned} \quad (4)$$

$$\mathcal{L} = \frac{1}{4} s^2 \bar{G} \lambda_0^4 B_{\perp}^2 \int_{\Delta\lambda} \left| \frac{\partial^2 I(\lambda)}{\partial \lambda^2} \right| d\lambda. \quad (5)$$

Our goal is to evaluate the expected errors  $\sigma_{B_{\parallel}}$  on  $B_{\parallel}$  and  $\sigma_{B_{\perp}}$  on  $B_{\perp}$  in some way that can be readily estimated, such as a function of the SNR of the intensity measurement that can be determined from a flux budget calculation. We therefore also define the integrated intensity signal,

$$\mathcal{I} = \int_{\Delta\lambda} I(\lambda) d\lambda, \quad (6)$$

and note that the uncertainties  $\sigma_{\mathcal{V}}$  of  $\mathcal{V}$  and  $\sigma_{\mathcal{L}}$  of  $\mathcal{L}$  are related to the uncertainty  $\sigma_{\mathcal{I}}$  of  $\mathcal{I}$  through the modulation efficiencies  $\epsilon_I$ ,  $\epsilon_Q$ ,  $\epsilon_U$ , and  $\epsilon_V$  in Stokes  $I$ ,  $Q$ ,  $U$ , and  $V$  (del

Toro Iniesta & Collados 2000),

$$\sigma_{\mathcal{V}} = \frac{\epsilon_I}{\epsilon_V} \sigma_{\mathcal{I}}, \quad (7)$$

$$\sigma_{\mathcal{L}} = \frac{\epsilon_I}{\epsilon_L} \sigma_{\mathcal{I}}, \quad (8)$$

where we have written  $\epsilon_L$  for the modulation efficiency of the linear polarization signal of interest.

Since Eq. 4 relates  $\mathcal{V}$  to  $B_{\parallel}$ , we can express the uncertainty  $\sigma_{B_{\parallel}}$  as the uncertainty of  $\mathcal{V}$ , and subsequently of  $\mathcal{I}$  by substituting Eq. 7,

$$\sigma_{B_{\parallel}} = \frac{1}{s \bar{g} \lambda_0^2} \left( \int_{\Delta\lambda} \left| \frac{\partial I(\lambda)}{\partial \lambda} \right| d\lambda \right)^{-1} \sigma_{\mathcal{V}} \quad (9)$$

$$= \frac{1}{s \bar{g} \lambda_0^2} \frac{\epsilon_I}{\epsilon_V} \left( \int_{\Delta\lambda} \left| \frac{\partial I(\lambda)}{\partial \lambda} \right| d\lambda \right)^{-1} \sigma_{\mathcal{I}}. \quad (10)$$

Note that we have used the property of the WFA that  $I$  does not depend on  $B$ . If we can express the integral of  $|\partial I(\lambda)/\partial \lambda|$  in terms of  $\mathcal{I}$ , then  $\sigma_{B_{\parallel}}$  can be expressed in the SNR of the intensity measurement,  $\mathcal{I}/\sigma_{\mathcal{I}}$ .

Equivalently, propagating the error in  $B_{\perp}$  through Eq. 5 and substituting Eq. 8, we find

$$\sigma_{B_{\perp}} = \frac{2}{s^2 \bar{G} \lambda_0^4} \frac{1}{B_{\perp}} \left( \int_{\Delta\lambda} \left| \frac{\partial^2 I(\lambda)}{\partial \lambda^2} \right| d\lambda \right)^{-1} \sigma_{\mathcal{L}} \quad (11)$$

$$= \frac{2}{s^2 \bar{G} \lambda_0^4} \frac{1}{B_{\perp}} \frac{\epsilon_I}{\epsilon_P} \left( \int_{\Delta\lambda} \left| \frac{\partial^2 I(\lambda)}{\partial \lambda^2} \right| d\lambda \right)^{-1} \sigma_{\mathcal{I}}. \quad (12)$$

In this case, we want to express the integral of  $|\partial^2 I/\partial \lambda^2|$  in terms of  $\mathcal{I}$ . We note, however, that  $\sigma_{B_{\perp}}$  is a function of  $B_{\perp}$ , and therefore the same SNR in  $\mathcal{I}$  will yield a different measurement error depending on the strength of the field being measured. Notably,  $\sigma_{B_{\perp}}$  is infinite for  $B_{\perp} = 0$ .

In practice,  $\mathcal{I}$  will be the sum of a series of discrete measurements. Each pixel samples the signal weighted with some point spread function, which causes cancellation of some amount of signal. This effect is discussed in more detail in Sect. 3. We assume here that the instrument is a spectrograph that samples the spectrum critically with a resolution  $R$ . However, the analysis for a different type of instrument, such as a wavelength-tunable imager, is analogous. The number of measurements  $N$  that spans the wavelength range  $\Delta\lambda$  is given by

$$N = \frac{2R \Delta\lambda}{\lambda_0}. \quad (13)$$

There are several ways to approach expressing the first and second derivatives of  $I(\lambda)$  in terms of itself. We will examine a simple approximation of the gradient in terms of the intensity and a characteristic wavelength interval, and a numeric calculation from simulated data or from observations of the intensity spectrum.

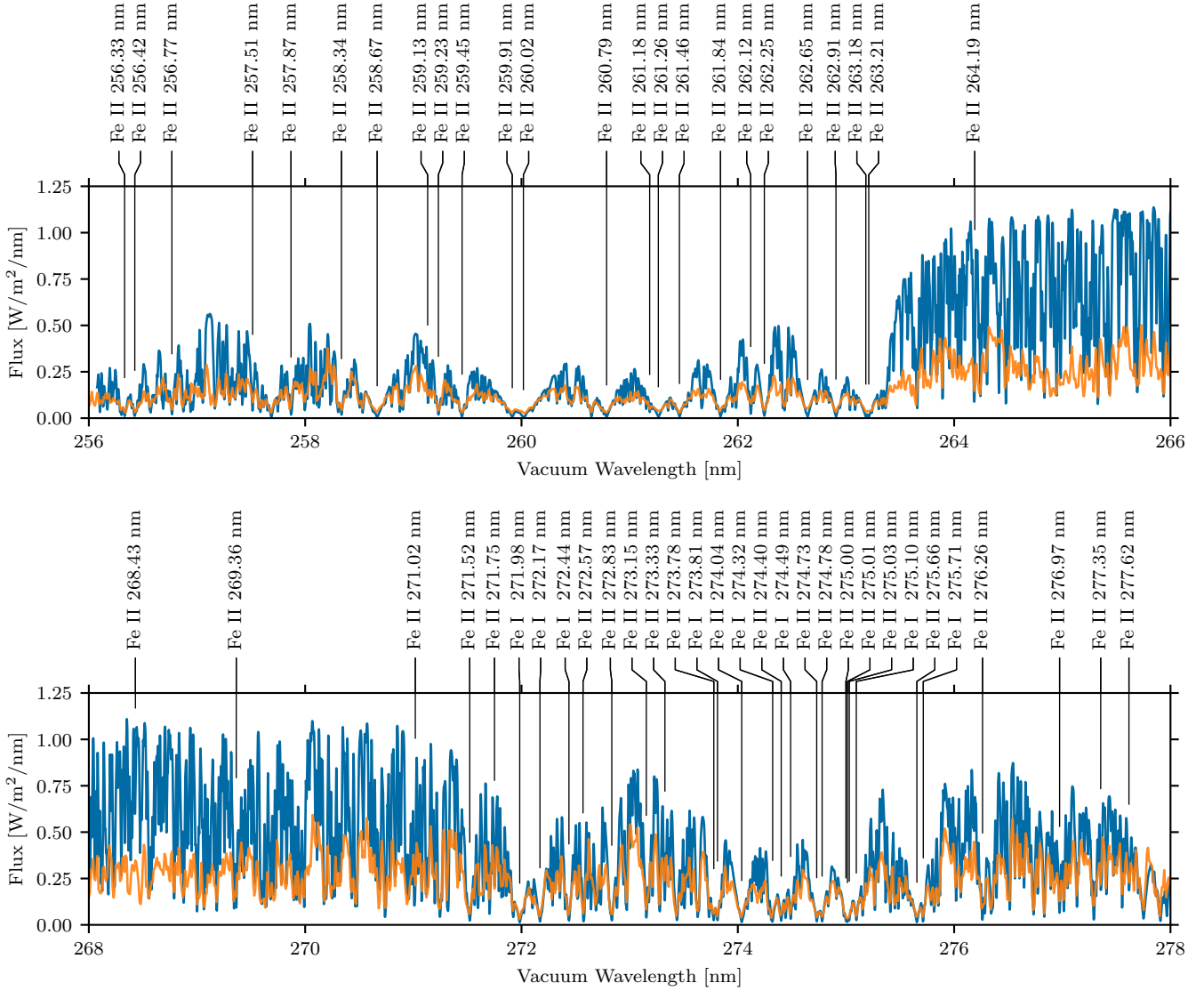


**Figure 1.** Blue lines: synthetic spectrum in two NUV windows that contain Fe I and Fe II lines of interest. Orange lines: measured flux from the 1983 Air Force Geophysics Laboratory (AFGL) balloon measurement. The synthetic spectrum shows very good agreement with the measured spectrum for the Fe I and Fe II lines.

### 2.1. Characteristic Wavelength Interval

This simple approximation equates the gradient as the ratio of the intensity and some characteristic wavelength interval,

$$\left| \frac{\partial I(\lambda)}{\partial \lambda} \right| \approx \frac{I(\lambda)}{\Delta \lambda}. \quad (14)$$

Substituting Eq. 14 in Eq. 10, we find

$$\sigma_{B\parallel} = \frac{\Delta \lambda}{s \bar{g} \lambda_0^2} \frac{\epsilon_I}{\epsilon_V} \frac{\sigma_I}{I}. \quad (15)$$

We approximate the pixel SNR,

$$I \approx \frac{1}{N} \mathcal{I}, \quad \sigma_I \approx \frac{1}{\sqrt{N}} \sigma_{\mathcal{I}}. \quad (16)$$

If the measurement noise is dominated by photon statistics, as is often the case, that property is preserved also for the average intensity  $I$ , i.e.,  $\sigma_I$  is approximately the square root of  $I$ , and therefore the SNR  $I/\sigma_I$  is the average SNR of the measurement over the wavelength range  $\Delta \lambda$ . Substitution of Eqs. 16 and 13 in Eq. 15 yields

$$\sigma_{B\parallel} = \frac{1}{s \bar{g} \lambda_0} \sqrt{\frac{\Delta \lambda}{2R \lambda_0}} \frac{\epsilon_I}{\epsilon_V} \frac{\sigma_I}{I}. \quad (17)$$

We apply this method to estimate the sensitivity of the Mg II h line. For this line, we have  $\bar{g} = 1.33$ , and  $\lambda_0 = 280$  nm. We estimate  $\Delta \lambda = 0.03$  nm (equivalent to a veloc-

ity of  $\pm 15 \text{ km s}^{-1}$ , see Eq. 25). We now find

$$\sigma_{B\parallel} = 7.58 \times 10^5 \frac{1}{\sqrt{R}} \frac{\sigma_I}{I} \text{ G.} \quad (18)$$

For example, if we evaluate this equation for a instrument with  $R = 30\,000$  and require  $\sigma_{B\parallel} \leq 8 \text{ G}$ , we find that the SNR in  $I$  must be at least 547.

## 2.2. Observed or Simulated Intensity Spectra

The estimation in Sect. 2.1 is obviously crude as it relies on a good estimate of  $\Delta\lambda$ , which is difficult without some prior knowledge of the line profile. A much better estimate can be derived from intensity spectra that were observed or computed with a numerical radiative transfer code such as RH (Uitenbroek 2001) or TURBOSPECTRUM (Alvarez & Plez 1998; Plez 2012) using a model atmosphere. We can numerically calculate the integral of the absolute value of the gradient as a fraction of  $\mathcal{I}$ ,

$$\gamma = \frac{1}{\mathcal{I}} \int_{\Delta\lambda} \left| \frac{\partial I(\lambda)}{\partial \lambda} \right| d\lambda, \quad (19)$$

Using again Eqs. 16 and 13, we now have

$$\sigma_{B\parallel} = \frac{1}{s \bar{g} \lambda_0^2} \frac{1}{\gamma} \sqrt{\frac{\lambda_0}{2\Delta\lambda}} \frac{\epsilon_I}{\sqrt{R} \epsilon_V} \frac{\sigma_I}{I}. \quad (20)$$

We now define the sensitivity factor for the error on the longitudinal field,

$$\Gamma = \gamma s \bar{g} \lambda_0^2 \sqrt{\frac{2\Delta\lambda}{\lambda_0}} \quad (21)$$

that captures the properties of a spectral line. Lines with larger  $\Gamma$  have higher sensitivity to longitudinal field, i.e., a requirement for a particular sensitivity of  $B_{\parallel}$  can be met with a measurement with lower SNR.

Similarly for the transverse component of the magnetic field we can numerically calculate the integral of the second derivative,

$$\chi = \frac{1}{\mathcal{I}} \int_{\Delta\lambda} \left| \frac{\partial^2 I(\lambda)}{\partial \lambda^2} \right| d\lambda, \quad (22)$$

and find

$$\sigma_{B\perp} = \frac{1}{s^2 \bar{G} \lambda_0^4} \frac{1}{\chi} \sqrt{\frac{2\lambda_0}{\Delta\lambda}} \frac{1}{B_{\perp}} \frac{\epsilon_I}{\sqrt{R} \epsilon_L} \frac{\sigma_I}{I}. \quad (23)$$

Therefore, we define the sensitivity factor for the error on the transverse field,

$$X = \chi s^2 \bar{G} \lambda_0^4 \sqrt{\frac{\Delta\lambda}{2\lambda_0}}. \quad (24)$$

We use the above procedure to calculate  $\Gamma$  and  $X$  for the lines listed in Judge et al. (2021) from a synthetic spectrum and observations from the IRIS mission (De Pontieu et al.

2014). Figure 1 shows the synthetic spectrum calculated with TURBOSPECTRUM from a custom Sun-like MARCS model atmosphere (Gustafsson et al. 2008) and using a line list adopted from the VALD database (Piskunov et al. 1995; Ryabchikova et al. 2015). This spectrum was calculated under the assumption of local thermal equilibrium (LTE), but shows very good agreement with measured spectra for the Fe I and Fe II lines, such as the AFGL balloon measurements (Hall & Anderson 1991) shown also in Fig. 1. The synthesis includes 102 691 lines from 115 atomic and 10 molecular species between 256 and 285 nm.

The MARCS model atmosphere does not include a chromospheric temperature rise. However, using a more realistic atmospheric model does not necessarily result in a more realistic synthetic spectrum. A model atmosphere like FAL-C (Fontenla et al. 1993) would result in emission peaks in the cores of strong lines that are not observed in the AFGL spectra. These peaks are the result of the assumption of LTE that is not valid in the line cores, and the peaks would not be present if non-LTE physics (e.g., scattering and partial redistribution) were included in the spectral synthesis.

We can expect the intensity in the cores of strong lines to saturate in this synthesis (see, e.g., the upper-left panel of Fig. 2). The resultant line core profile is nearly flat and exhibits only a small gradient and second derivative, and hence little circular or linear polarization signal is produced in the presence of magnetic field. Therefore, the analysis presented here based on this synthesis will produce lower values of  $\Gamma$  and  $X$  than one based on a synthesis that incorporates pertinent non-LTE effects and uses a more realistic atmospheric model.

IRIS observes the solar spectrum around the Mg II h and k lines that also includes the Mn I lines used by Ishikawa et al. (2021) to infer longitudinal magnetic field from data from the CLASP2 flight (Narukage et al. 2016; Tsuzuki et al. 2020). We choose a data set of NOAA AR12957 taken on March 4, 2022 around 10 UT. This observation contains a region of plage, the edge of a sunspot, and some more quiet areas. The left panel of Fig. 3 shows the intensity of the Mg II k core. We could compute the longitudinal and transverse sensitivity factors for every pixel in the map. However, we would overestimate the factors due to measurement noise that creates spurious signals in first and second derivative of the intensity profile. We therefore use “representative profiles” (RPs) from the IRIS<sup>2</sup> database (Sainz Dalda et al. 2019). An RP is an average of many similar line profiles, and therefore has very low noise, so that we can accurately determine the first and second derivative of the intensity. There are 160 RPs in this map. More than half the pixels are represented by the most popular 25 RPs, and only 3 RPs represent less than 100 pixels each.

We note that we can express  $\Delta\lambda$  in terms of a velocity  $v$ ,

$$\Delta\lambda = 2 \frac{v}{c} \lambda_0. \quad (25)$$

We use  $v = 12.5 \text{ km s}^{-1}$  for the Fe I, Fe II, and Mg II lines, and  $v = 7.5 \text{ km s}^{-1}$  for the Mn I lines. These velocities give reasonable integration intervals and more or less correspond to typical sound speed estimates for the chromosphere and

photosphere. The values for  $\Gamma$  and  $X$  are not strongly dependent on the choice of  $v$ , since the wings of the lines tend not to contribute significant polarization signal (see Fig. 2). However, other nearby spectral lines may contribute spurious polarization signal in the wavelength window. We therefore limit the window to the nearest local maximum of the intensity spectrum to reduce contamination by other lines (see Fig. 2 panels in the middle row left and center column).

**Table 1.** Longitudinal and transverse field sensitivity factors for prominent lines in the solar chromospheric spectrum.  $\Delta\lambda$  denotes the integration window. Landé  $g$ -factors are computed using LS coupling. Wavelength in air is included for easy reference against Table 1 in Judge et al. (2021).

$\lambda_0$ (nm)	$\lambda_{0,\text{air}}$ (nm)	$\Delta\lambda$ (pm)	Ion	$\log \tau_0$	$g$	$\Gamma$ ( $10^{-5} \text{ G}^{-1}$ )	$G$	$X$ ( $10^{-8} \text{ G}^{-2}$ )	Blend
256.331	256.408	-11/ + 7	Fe II	-2.54	1.21	1.17	1.46	2.45	minor
256.425	256.502	-5/ + 8	Fe II	-2.87	1.10	1.21	1.18	2.86	major
256.768	256.845	$\pm 11$	Fe II	-3.30	0.83	0.94	0.56	1.15	
257.514	257.591	$\pm 11$	Fe II	-4.33	1.30	1.77	1.65	3.03	minor
257.869	257.946	-11/ + 6	Fe II	-3.32	1.33	1.53	-0.01	0.01	major
258.335	258.413	$\pm 11$	Fe II	-3.19	1.47	1.62	1.74	3.59	
258.665	258.743	$\pm 11$	Fe II	-2.03	1.50	0.73	2.25	1.00	minor
259.132	259.210	-11/ + 10	Fe II	-4.47	1.50	1.71	2.25	4.27	severe
259.232	259.309	-8/ + 11	Fe II	-3.24	1.49	1.61	2.03	4.08	minor
259.451	259.528	-8/ + 11	Fe II	-4.02	2.17	1.80	4.52	7.14	minor
259.915	259.992	$\pm 11$	Fe II	-1.93	1.50	0.73	2.25	0.75	
260.018	260.095	$\pm 11$	Fe II	-1.39	1.56	0.42	2.42	0.30	minor
260.787	260.865	$\pm 11$	Fe II	-1.99	1.50	0.82	2.24	1.28	minor
261.185	261.263	-11/ + 6	Fe II	-4.23	1.90	2.30	3.58	9.01	minor
261.265	261.343	$\pm 11$	Fe II	-1.79	1.59	0.73	2.52	0.83	
261.460	261.538	$\pm 11$	Fe II	-2.20	1.50	0.94	2.12	1.54	
261.840	261.918	$\pm 11$	Fe II	-2.36	1.66	1.13	2.75	2.42	
262.119	262.197	-11/ + 5	Fe II	-3.75	1.87	2.31	3.49	9.82	major
262.245	262.323	$\pm 11$	Fe II	-2.76	3.34	3.10	11.15	17.84	
262.645	262.724	$\pm 11$	Fe II	-2.08	1.50	0.98	2.25	1.75	
262.907	262.986	$\pm 11$	Fe II	-2.21	1.50	1.04	2.12	1.79	
263.183	263.262	-11/ + 10	Fe II	-2.02	1.50	0.85	2.24	1.44	major
263.210	263.289	$\pm 11$	Fe II	-1.97	1.50	0.81	2.25	1.41	major
264.191	264.269	-6/ + 11	Fe II	-4.62	1.87	2.61	3.39	13.36	severe
268.431	268.510	-4/ + 2	Fe II	-4.99	1.84	0.64	3.34	2.76	severe
269.363	269.443	-8/ + 11	Fe II	-4.40	1.93	3.42	3.64	10.36	major
271.018	271.099	-4/ + 11	Fe II	-4.30	2.10	3.53	4.17	19.21	severe
271.521	271.602	$\pm 11$	Fe II	-3.09	1.50	1.53	2.25	3.82	
271.751	271.831	$\pm 5$	Fe II	-3.11	1.33	2.83	1.55	8.63	severe

**Table 1** continued

**Table 1** (*continued*)

$\lambda_0$ (nm)	$\lambda_{0,\text{air}}$ (nm)	$\Delta\lambda$ (pm)	Ion	$\log \tau_0$	$g$	$\Gamma$ ( $10^{-5} \text{ G}^{-1}$ )	$G$	$X$ ( $10^{-8} \text{ G}^{-2}$ )	Blend
271.984	272.064	$\pm 11$	Fe I	-4.45	1.25	0.92	1.54	1.77	minor
272.171	272.251	$\pm 11$	Fe I	-4.76	1.17	1.07	1.32	2.31	
272.439	272.519	-8/ + 11	Fe I	-5.22	1.00	1.08	0.85	1.67	minor
272.569	272.649	-11/ + 4	Fe II	-3.05	1.20	1.38	1.03	2.48	severe
272.835	272.916	$\pm 11$	Fe II	-3.05	1.50	1.47	2.25	4.19	minor
273.154	273.235	$\pm 11$	Fe II	-3.19	0.80	0.97	-0.29	0.64	
273.326	273.407	-9/ + 10	Fe II	-4.92	1.45	2.63	1.60	5.32	major
273.778	273.859	-6/ + 11	Fe II	-3.22	1.50	1.61	2.16	4.88	severe
273.812	273.893	$\pm 11$	Fe I	-5.12	2.00	2.08	3.26	7.55	
274.036	274.117	$\pm 11$	Fe II	-3.31	1.43	1.05	2.04	2.02	minor
274.322	274.403	-5/ + 11	Fe I	-5.01	1.67	1.55	2.52	5.56	severe
274.401	274.482	$\pm 11$	Fe II	-2.81	0.50	0.47	0.24	0.39	
274.488	274.569	$\pm 11$	Fe I	-5.51	2.50	2.78	6.27	15.09	
274.729	274.810	$\pm 11$	Fe II	-2.59	0.90	0.77	0.80	1.15	
274.779	274.861	$\pm 11$	Fe II	-2.66	1.37	1.17	1.88	2.54	
274.999	275.081	-11/ + 6	Fe II	-3.02	1.20	1.03	1.44	2.84	severe
275.013	275.095	-8/ + 11	Fe II	-2.38	1.07	0.80	1.14	1.69	severe
275.030	275.112	-5/ + 11	Fe II	-3.24	0.00	0.00	0.00	0.00	severe
275.095	275.177	$\pm 11$	Fe I	-5.04	1.58	1.65	2.38	5.64	minor
275.655	275.737	$\pm 11$	Fe II	-2.17	1.17	0.85	1.35	1.23	
275.714	275.796	-4/ + 11	Fe I	-5.52	2.00	1.71	3.99	8.45	severe
276.263	276.344	-12/ + 7	Fe II	-3.25	1.50	1.89	2.16	5.01	major
276.975	277.057	-7/ + 12	Fe II	-3.08	1.50	2.26	2.25	5.84	severe
277.355	277.437	-6/ + 5	Fe II	-3.14	1.50	2.86	2.25	9.38	severe
277.616	277.698	-6/ + 4	Fe II	-6.06	1.34	2.36	0.44	1.84	severe
279.564	279.647	$\pm 7$	Mn I	-5.65	1.98	0.64	1.80	0.42	minor
279.635	279.718	$\pm 12$	Mg II	0.00	1.17	0.27	1.33	0.13	
279.909	279.992	$\pm 7$	Mn I	-5.79	1.70	1.01	3.74	1.44	
280.191	280.273	$\pm 7$	Mn I	-5.96	0.84	0.48	2.85	1.09	
280.353	280.435	$\pm 12$	Mg II	-0.30	1.33	0.31	1.33	0.15	

Results are given in Table 1 and shown in Figs. 3 and 4. The line profiles were visually evaluated and qualitatively categorized as suffering from blends with varying severity given in the “Blend” column. The  $\Gamma$  and  $X$  values of a line with a major or severe blend are likely affected and overestimate the true values, as the blends create additional gradients. The values for the Mg II and Mn I lines in the table are derived from the spectrum of the most popular RP that represents 10 697 pixels (3.2% of the FOV). We processed each RP, and map the longitudinal and transverse sensitivity factors back to pixels in the FOV, shown in the center and right

panels of Fig. 3, respectively. Figure 4 shows the cumulative probability density functions for the longitudinal and transverse sensitivity factors. The most popular RP is around the 70% and 85% percentiles for  $\Gamma$  and  $X$ , respectively.

We select a series of Fe II lines, a single Fe I line, and the Mg II h and k lines for closer study. We pick Fe I and Fe II lines that are preferentially unaffected by blends, sample at optical depths down to the photosphere in roughly equal steps of  $\log \tau$ , have large  $\Gamma$  and  $X$ , and are nearby one another in the spectrum. This selection procedure results nine lines in two distinct wavelength regions of interest: between Fe II 260.018 nm and Fe II 262.245 nm, and between Fe I 274.488 nm and Mg II h 280.353 nm. Figure 2 shows the

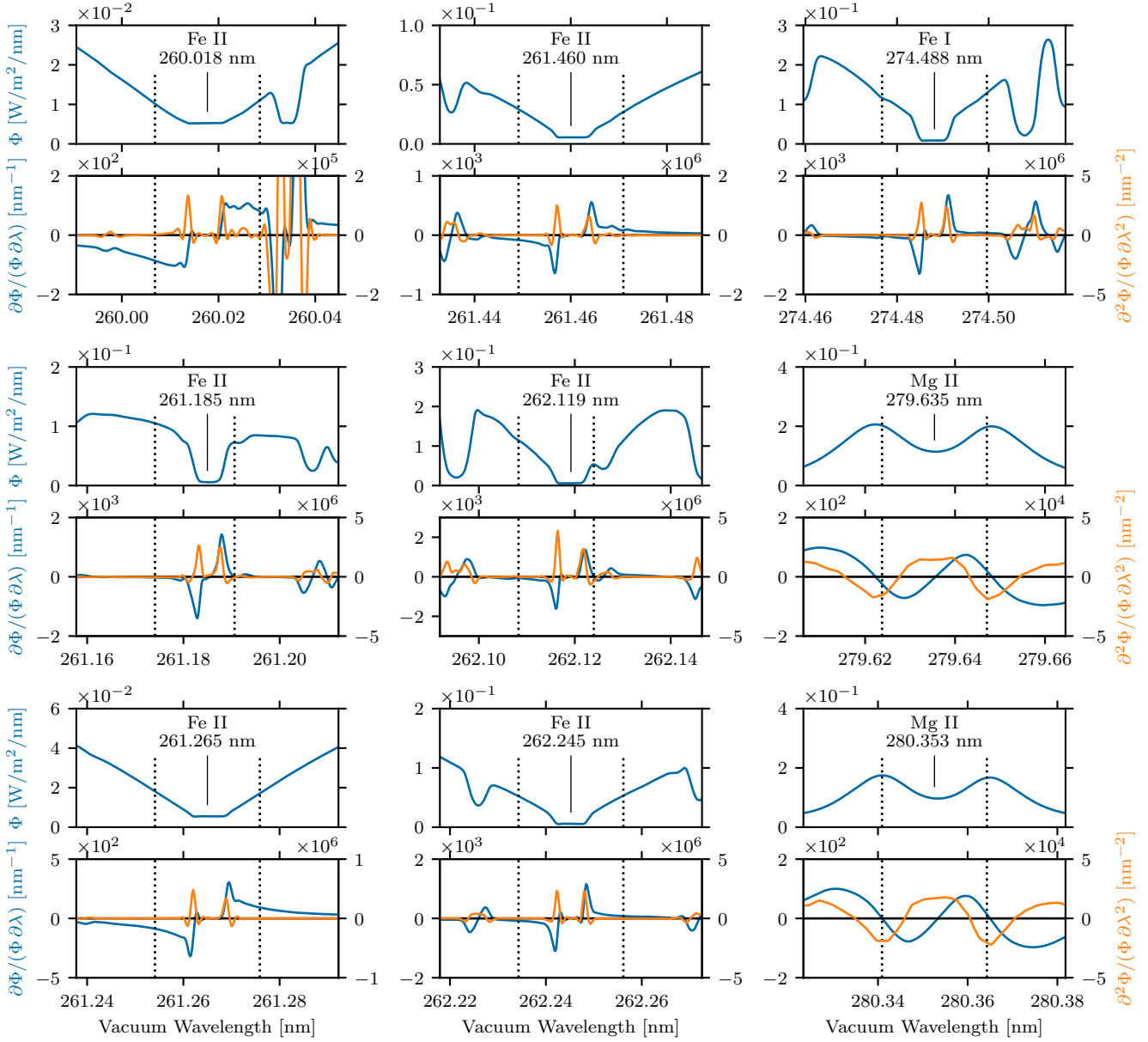


**Figure 2.** Intensity, and first and second derivative of intensity for selected lines.

synthetic spectra for these lines, together with the first and second derivatives.

### 3. Instrumental Effects

In practice, all measurements will be affected by instrumental effects. As already mentioned in Sect. 2,  $\mathcal{I}$  will be the sum of a series of discrete measurements that sample the signal weighted with some line spread function (LSF). We evaluate here how this affects the required measurement sensitivity. For the sake of simplicity, we assume each measurement is affected by the same LSF  $\rho(\lambda)$ . Equations 6, 19, and

22 then become

$$\mathcal{I}' = \int_{\Delta\lambda} (\rho * I)(\lambda) d\lambda, \quad (26)$$

$$\gamma' = \frac{1}{\mathcal{I}'} \int_{\Delta\lambda} \left| \left( \rho * \frac{\partial I}{\partial \lambda} \right) (\lambda) \right| d\lambda, \quad (27)$$

$$\chi' = \frac{1}{\mathcal{I}'} \int_{\Delta\lambda} \left| \left( \rho * \frac{\partial^2 I}{\partial \lambda^2} \right) (\lambda) \right| d\lambda, \quad (28)$$

where  $*$  denotes convolution. It is straightforward to implement this in the numerical analysis presented in Sect. 2.2.

The LSF of a spectrograph depends on its specific configuration (Casini & de Wijn 2014). The LSF of a typical spec-

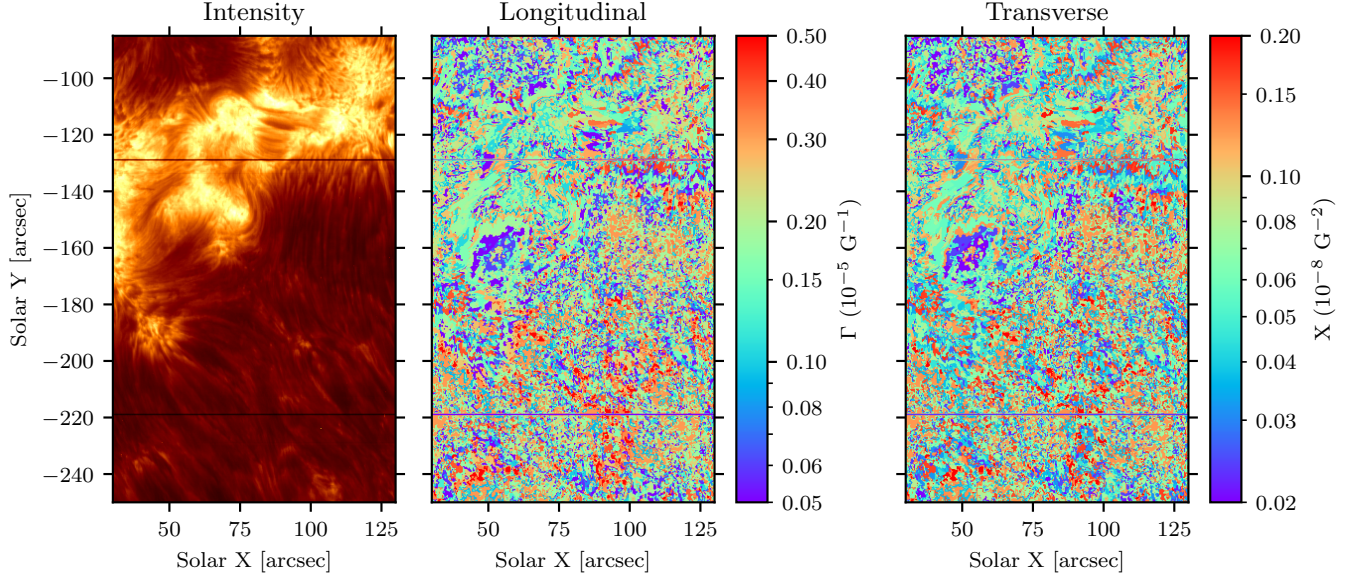


**Figure 3.** IRIS map used to calculate the longitudinal and transverse sensitivity factors for Mg II and Mn I lines. Left panel: intensity in the core of the Mg II k line. Center panel: longitudinal field sensitivity factor  $\Gamma$ . Right panel: transverse field sensitivity factor  $X$ .

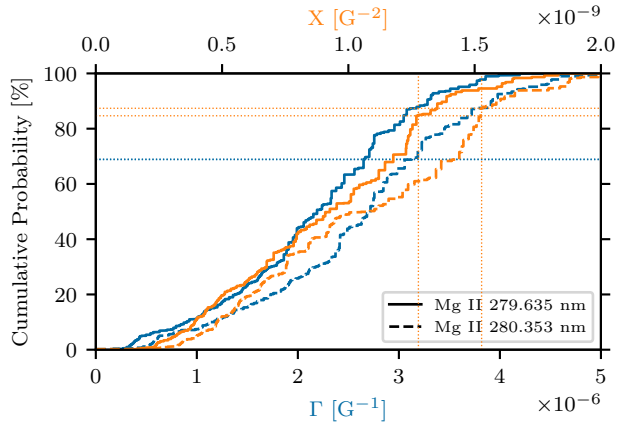


**Figure 4.** Cumulative distribution function of the longitudinal and transverse sensitivity factors  $\Gamma$  and  $X$  for the Mg II h and k lines. The  $\Gamma$  and  $X$  values and the cumulative probabilities for the most popular RP (also given in Table 1) are indicated by vertical and horizontal dotted lines, respectively.

trograph operating in Littrow condition that also satisfies the “pixel-matching” condition, i.e., the projected width of the slit is equal to the width of a camera pixel, is approximately Gaussian after accounting for sampling. We therefore choose to model the LSF as a Gaussian function.

Signal loss factors are shown as a function of spectral resolution for a collection of Fe I and Fe II lines and the Mg II lines in Fig. 5. Stokes  $V$  signals are less affected than linear polarization signals at reasonable spectral resolution. Lin-

ear polarization signal loss varies considerably from line to line, but generally lines that form deeper in the atmosphere have narrower profiles that require higher spectral resolution to achieve the same loss factor. The Fe II 260.018 nm line is affected by a blend that at spectral resolutions below about 40 000 starts to contaminate the polarization signal, causing a spurious rise in the  $L$  signal loss factor.

#### 4. Example SNR Calculation

We now show an example using the above calculations to derive measurement requirements, i.e., SNR on Stokes  $I$ , for a hypothetical instrument that observes the nine spectral lines previously selected.

Substituting  $\gamma'$  and  $\chi'$  for  $\gamma$  and  $\chi$  in Eqs. 21 and 24 to account for instrument spectral resolution yields

$$\Gamma' = 2\gamma' s \bar{g} \lambda_0^2 \sqrt{\frac{v}{c}} \quad (29)$$

$$X' = \chi' s^2 \bar{G} \lambda_0^4 \sqrt{\frac{v}{c}}. \quad (30)$$

The errors on the longitudinal and transverse magnetic field are given by

$$\sigma_{B\parallel} = \frac{1}{\Gamma'} \frac{\epsilon_I}{\sqrt{R} \epsilon_V} \frac{\sigma_I}{I}, \quad (31)$$

$$\sigma_{B\perp} = \frac{1}{X'} \frac{1}{B_\perp} \frac{\epsilon_I}{\sqrt{R} \epsilon_L} \frac{\sigma_I}{I}. \quad (32)$$

We assume the instrument has a spectral resolution of 30 000 and calculate  $\Gamma'$  and  $X'$  for spectral lines of interest.



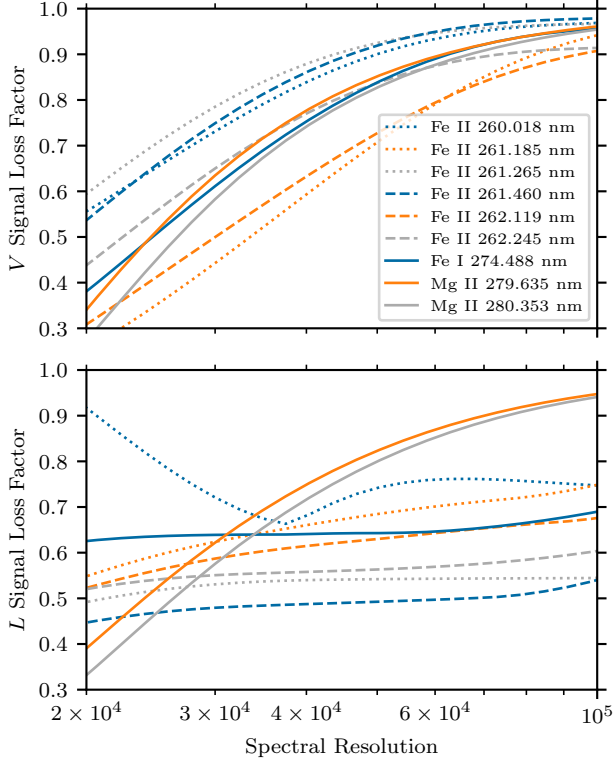


**Figure 5.** Signal loss factor of SNR resulting from instrumental smearing as a function of the instrument spectral resolution.

A reasonable estimate for a near-optimal, balanced modulator is  $\epsilon_I/\epsilon_V \approx \epsilon_I/\epsilon_L \approx 1.8$  (e.g., Tomczyk et al. 2010). We thus set the factors  $\epsilon_I/(\sqrt{R}\epsilon_V)$  and  $\epsilon_I/(\sqrt{R}\epsilon_L)$  to be equal to 0.01. Finally, we have to estimate  $B_\perp$  in order to evaluate Eq. 32. We choose a stepped function for  $B_\perp$  starting at 200 G at the top of the chromosphere to 50 G in the photosphere based on simulations of a magnetic flux rope and a sheared arcade (M. Rempel, private communication). As an example, we calculate the required SNR  $\sigma_I/I$  required to detect the transverse field and a 20 G longitudinal field with  $2.5\sigma$  significance. The results are summarized in Table 2. We note that the SNR values are the average pixel SNR over the spectral window between the vertical dotted lines in the panels of Fig. 2. Generally, we observe that lines that form higher in the atmosphere require higher SNR. To demonstrate that these SNR requirements are achievable, we also calculate the SNR of a 12 s integration by such a hypothetical instrument with a 30 cm aperture, 2.5% throughput, and  $1''$  spatial resolution. The deep Fe II line at 260.018 nm drives the instrument requirements. The Mg II lines achieve higher SNR than that line because of the increased intensity in the 2V and 2R peaks.

**Table 2.** Required SNR to detect magnetic field with  $2.5\sigma$  significance. Case 1: detection of transverse field with strength  $B_\perp$ . Case 2: detection of  $B_\parallel = 20$  G. The Instrument column lists the projected performance of a hypothetical instrument. See text for details.

$\lambda_0$	Ion	$\log \tau_0$	$B_\perp$	Case 1	Case 2	Instrument
260.018	Fe II	-1.39	150	539	419	553
261.185	Fe II	-4.23	50	185	127	771
261.265	Fe II	-1.79	150	263	228	644
261.460	Fe II	-2.20	100	351	184	581
262.119	Fe II	-3.75	75	80	112	955
262.245	Fe II	-2.76	100	26	65	700
274.488	Fe I	-5.51	50	108	76	971
279.635	Mg II	0.00	200	818	768	1593
280.353	Mg II	-0.30	200	739	724	1436

## 5. Conclusion

We have investigated the lines in the wavelength region between about 250 and 290 nm identified by Judge et al. (2021) as being optimal for studying magnetism in the solar chromosphere. We have derived equations and procedures to quantify the sensitivity of spectral lines to magnetic field through the Zeeman effect based on observed or synthetic intensity spectra. While we have applied these methods to the spectral region suggested by Judge et al. (2021), they are applicable to any spectral line.

An example calculation shows that observations with an instrument with a spectral resolution of 30 000 need to reach achievable Stokes- $I$  SNR ratios of a few hundred, which are achievable for an instrument with a 30 cm aperture and 2.5% throughput at  $1''$  spatial resolution with an integration time of 12 s. We thus conclude that this region of the solar spectrum in the near-UV yields observable polarization signals with suitable diagnostic potential for studies of chromospheric magnetism through the Zeeman effect.

We have not evaluated the *interpretability* of observations of these lines. That work requires a more complex approach of synthesizing spectra from known model atmospheres, degrading those spectra as if they were observed by a hypothetical instrument, and attempting to recover the model parameters through interpretation using the WFA or with inversion codes like DeSIRE (Ruiz Cobo et al. 2022), STiC (de la Cruz Rodríguez et al. 2019), or TIC (Li et al. 2022). The Mg II lines have been studied and used for diagnostics of chromospheric magnetism in recent years (e.g., del Pino Alemán et al. 2016; Manso Sainz et al. 2019; Ishikawa et al. 2021; Centeno et al. 2022; Rachmeler et al. 2022; Afonso Delgado et al. 2023a; Li et al. 2023) These efforts should be continued and expanded to include the Fe I and Fe II lines

identified in this work. A first step in this direction was recently taken by Afonso Delgado et al. (2023b), who studied the magnetic sensitivity of Fe II between 250 and 278 nm using a many-level model atom and realistic physics using the HanleRT code. They note that observations of the solar spectrum are required to study the effects of UV line blanketing and validate the atomic data, in particular the rate of inelastic collisions with electrons. We assert based on the results presented in this paper that this region of the solar spectrum holds great promise and instrumentation to observe it should be developed.

*CRedit author statement*—Investigation: A.G. de Wijn, P.G. Judge, R. Ezzeddine, A. Sainz Dalda; Writing—original draft preparation: A.G. de Wijn; Writing—review and editing: P.G. Judge.

### Acknowledgments

This material is based upon work supported by the National Center for Atmospheric Research, which is a major facility sponsored by the National Science Foundation under Cooperative Agreement No. 1852977. AdW acknowledges support by the National Aeronautics and Space Ad-

ministration under Grant 80NSSC21K1792 issued through the Heliophysics Flight Opportunity Studies program. R.E. acknowledges support from NSF grant AST-2206263. IRIS is a NASA small explorer mission developed and operated by LMSAL with mission operations executed at NASA Ames Research Center and major contributions to downlink communications funded by ESA and the Norwegian Space Centre. This work has made use of the VALD database, operated at Uppsala University, the Institute of Astronomy RAS in Moscow, and the University of Vienna. The following acknowledgements were compiled using the Astronomy Acknowledgement Generator (<https://astrofrog.github.io/acknowledgment-generator/>). This research has made use of NASA's Astrophysics Data System, NumPy (van der Walt et al. 2011), matplotlib, a Python library for publication quality graphics (Hunter 2007), SciPy (Virtanen et al. 2020), and the IPython package (Perez & Granger 2007).

### Comments

This version of the article has been accepted for publication after peer review but is not the Version of Record and does not reflect post-acceptance improvements, or any corrections. The Version of Record is available online at <https://doi.org/10.3847/1538-4357/ace041>.

### REFERENCES

- Afonso Delgado, D., del Pino Alemán, T., & Trujillo Bueno, J. 2023a, *ApJ*, 942, 60
- Afonso Delgado, D., del Pino Alemán, T., & Trujillo Bueno, J. 2023b, *ApJ*, 948, 86
- Alvarez, R. & Plez, B. 1998, *A&A*, 330, 1109
- Casini, R. & de Wijn, A. G. 2014, *Journal of the Optical Society of America A*, 31, 2002
- Centeno, R., Rempel, M., Casini, R., & del Pino Alemán, T. 2022, *ApJ*, 936, 115
- de la Cruz Rodríguez, J., Leenaarts, J., Danilovic, S., & Uitenbroek, H. 2019, *A&A*, 623, A74
- De Pontieu, B., Title, A. M., Lemen, J. R., et al. 2014, *SoPh*, 289, 2733
- del Pino Alemán, T., Casini, R., & Manso Sainz, R. 2016, *ApJL*, 830, L24
- del Pino Alemán, T., Trujillo Bueno, J., Casini, R., & Manso Sainz, R. 2020, *ApJ*, 891, 91
- del Toro Iniesta, J. C. & Collados, M. 2000, *ApOpt*, 39, 1637
- Fontenla, J. M., Avrett, E. H., & Loeser, R. 1993, *ApJ*, 406, 319
- Gustafsson, B., Edvardsson, B., Eriksson, K., et al. 2008, *A&A*, 486, 951
- Hall, L. A. & Anderson, G. P. 1991, *J. Geophys. Res.*, 96, 12,927
- Hunter, J. D. 2007, *Computing in Science and Engineering*, 9, 90
- Ishikawa, R., Bueno, J. T., del Pino Alemán, T., et al. 2021, *Science Advances*, 7, eabe8406
- Judge, P., Rempel, M., Ezzeddine, R., et al. 2021, *ApJ*, 917, 27
- Landi Degl'Innocenti, E. & Landi Degl'Innocenti, M. 1973, *SoPh*, 31, 299
- Landi Degl'Innocenti, E. & Landolfi, M. 2004, *Polarization in Spectral Lines*, Vol. 307 (Springer, Dordrecht)
- Li, H., del Pino Alemán, T., Trujillo Bueno, J., & Casini, R. 2022, *ApJ*, 933, 145
- Li, H., del Pino Alemán, T., Trujillo Bueno, J., et al. 2023, *ApJ*, 945, 144
- Manso Sainz, R., del Pino Alemán, T., Casini, R., & McIntosh, S. 2019, *ApJL*, 883, L30
- Narukage, N., McKenzie, D. E., Ishikawa, R., et al. 2016, in *Society of Photo-Optical Instrumentation Engineers (SPIE) Conference Series*, Vol. 9905, *Space Telescopes and Instrumentation 2016: Ultraviolet to Gamma Ray*, ed. J.-W. A. den Herder, T. Takahashi, & M. Bautz, 990508
- Perez, F. & Granger, B. E. 2007, *Computing in Science and Engineering*, 9, 21
- Piskunov, N. E., Kupka, F., Ryabchikova, T. A., Weiss, W. W., & Jeffery, C. S. 1995, *A&AS*, 112, 525
- Plez, B. 2012, *Turbospectrum: Code for spectral synthesis*, *Astrophysics Source Code Library*, record ascl:1205.004

- Rachmeler, L. A., Trujillo Bueno, J., McKenzie, D. E., et al. 2022, *ApJ*, 936, 67
- Ruiz Cobo, B., Quintero Noda, C., Gafeira, R., et al. 2022, *A&A*, 660, A37
- Ryabchikova, T., Piskunov, N., Kurucz, R. L., et al. 2015, *PhysS*, 90, 054005
- Sainz Dalda, A., de la Cruz Rodríguez, J., De Pontieu, B., & Gošić, M. 2019, *ApJL*, 875, L18
- Tomczyk, S., Casini, R., de Wijn, A. G., & Nelson, P. G. 2010, *ApOpt*, 49, 3580
- Tsuzuki, T., Ishikawa, R., Kano, R., et al. 2020, in *Society of Photo-Optical Instrumentation Engineers (SPIE) Conference Series*, Vol. 11444, Society of Photo-Optical Instrumentation Engineers (SPIE) Conference Series, 114446W
- Uitenbroek, H. 2001, *ApJ*, 557, 389
- van der Walt, S., Colbert, S. C., & Varoquaux, G. 2011, *Computing in Science and Engineering*, 13, 22
- Virtanen, P., Gommers, R., Oliphant, T. E., et al. 2020, *Nature Methods*, 17, 261